Available online at www.sciencedirect.com

ScienceDirect

Journal of Magnesium and Alloys 8 (2020) 374–386

www.elsevier.com/locate/jma

Full Length Article

A novel biodegradable Mg-1Zn-0.5Sn alloy: Mechanical properties, corrosion behavior, biocompatibility, and antibacterial activity

Weikang Zhao[a,d,e], Jingfeng Wang[b,*], Jiang Weiyang[b], Bo Qiao[a], Yiyang Wang[d], Yuling Li[c,*], Dianming Jiang[a,d,*]

[a] Department of Orthopedics, The First Affiliated Hospital of Chongqing Medical University, Chongqing 400016, PR China
[b] National Engineering Research Center for Magnesium Alloys, College of Materials Science and Engineering, Chongqing University, Chongqing 400044, PR China
[c] Department of Orthopedics, Affiliated Hospital of North Sichuan Medical College, Sichuan 637000, PR China
[d] Department of Orthopedics, Third Affiliated Hospital of Chongqing Medical University, Chongqing 401120, PR China
[e] Department of Bioengineering, University of California, Los Angeles, California 90095-1600, United States

Received 1 December 2019; received in revised form 6 February 2020; accepted 13 February 2020
Available online 13 May 2020

Abstract

To meet the growing demand for antibacterial implants for bone-implant-associated infection therapy and avoid the adverse effects of secondary surgery, a degradable platform with pH responsiveness and ion-associated antibacterial properties was constructed. A small amount of Sn added to Mg-1Zn alloy reduces the biocorrosion rate, which can be attributed to Sn participation in outer-layer film formation, significantly reducing the biocorrosion rate and hydrogen evolution rate after implantation *in vivo*. These Mg alloys, which are susceptible to degradation in the acidic bacterial microenvironment, degrade by releasing Mg, Zn and Sn, producing favorably alkaline and antibacterial conditions. Samples with the composition of Mg-1Zn-0.5Sn were found to be beneficial for promoting initial cell adhesion and proliferation, resulting in improved biocompatibility and biosafety. The biocompatibility of this alloy was confirmed by the healthy behavior of animals and the absence of acute or chronic toxicity in the liver, spleen, and kidneys. Our results demonstrate that Mg-1Zn-0.5Sn is safe for biological systems, enabling its efficacious use in biomedical applications.

Keywords: Magnesium alloy; Degradable materials; Antibacterial; Biosafety.

1. Introduction

The demand for artificial organs and other biomedical devices has increased drastically during recent decades. Commonly used high-performance implant materials include stainless steel (SS), cobalt-chromium (Co–Cr) and titanium (Ti) and their alloys/composites [1]. However, certain drawbacks suggest that their full potential may nearly be exhausted. First, the Young's moduli of the aforementioned materials (110–200 GPa) are higher than that of bone (7–25 GPa), which causes stress shielding [2,3]. As a result, bone resorption occurs, leading to implant loosening and failure [4]. Second, due to the adverse effects of nondegradable materials, the feasibility of developing biodegradable materials has attracted strong interest. Recently, magnesium (Mg) and its alloys have gained a great deal of attention as promising and potential biodegradable materials for the fabrication of bone fixation accessories because of their favorable biological properties [5–7].

Mg implants can be dissolved, absorbed and/or excreted, so that implant removal surgery is not required [8]. However, one major the concern with Mg is its high corrosion rate, making it unpredictable in the physiological environment [9–11].

* Corresponding author.
E-mail addresses: weikang-zhao@cqu.edu.cn (W. Zhao), jfwang@cqu.edu.cn (J. Wang), lyl1987@nsmc.edu.cn (Y. Li), jdm571026@vip.163.com (D. Jiang).

https://doi.org/10.1016/j.jma.2020.02.008

In fact, Mg is electrochemically very active, with a standard potential of −2.7 V (Mg/Mg^{2+}, standard hydrogen potential) [12]. Fast corrosion results in implant failure before a bone fracture is healed. Bone healing process normally takes over 3 months while currently available biodegradable Mg alloys cannot maintain their mechanical integrity within this time frame [13]. Another problem is about corrosion products of Mg, i.e. hydrogen gas (H_2) bubbles which form around the implant [14,15]. The H_2 bubbles evolved from a corroding Mg implant can be accumulated in the form of gas pockets in the tissues surrounding the implant, which may ultimately lead to the separation of tissue layers and tissue necrosis [16]. In a worst-case scenario, patient death is possible if a large amount of H_2 bubbles diffuse through the blood circulating system and block blood stream. Decreasing the corrosion rate of Mg alloys is the only way to solve the problem. At a decreased corrosion rate, Mg_2+ ions, H_2 bubbles and $OH-$ ions will be produced more slowly, allowing the host tissue to gradually adjust or deal with the biodegradation products [17].

Extensive research has been done to decrease the Mg's corrosion rate [18,19], including new alloy development [17], tailoring the microstructure or the surface properties [20,21], reinforcing with bioceramic particles [22], thermomechanical processing [23] and coating them with biopolymers [24] and/or bioceramics [25] using different coating techniques such as electrodeposition [3], electrophoretic deposition [26] and dip-coating [27] Elemental alloying has been reported as the most effective technique to improve the corrosion resistance and mechanical properties of Mg alloys [28]. Zinc, with its standard corrosion potential (−0.8 V vs. standard hydrogen electrode (SHE)) between that of magnesium (−2.37 V vs. SHE) and iron (−0.4 V vs. SHE), is a promising candidate as a biodegradable metal [29,30]. As an essential nutrient of the human body, Zinc (Zn) reduces the implant corrosion rate and improves its mechanical strength [30]. Moreover, the low concentrations of Zn involved are known to be biologically safe [31]. Mg-1Zn alloy with a microstructure of a single solid solution was found to present satisfactory biocompatibility and to produce less hydrogen gas than many other binary Mg alloys in simulated body fluid [32]. However, the mechanical properties and degradation rate should be further enhanced for practical clinical application [26,33–35].

Moreover, due to the high solubility in Mg, the addition of Zn could lead to a continuous increase in yield strength (YS) as Zn increases from 1 to 6 wt.%. However, the effect of zinc content on the microstructure and corrosion behavior was revealed that higher Zn content led to a reduction in the grain size and an increase in the amount of second phase ($MgZn_2$). That was to say, the increase of strength was in conflict with the decrease of corrosion rate. Since reducing corrosion rate is the most important goal of magnesium alloy biomaterials, this experiment limits the Zn content to 1 wt%.% [7,36].

However, to meet the clinical demand, both the mechanical and corrosion properties still needs to be further improved. Tin (Sn), another essential trace element in the human body, has a high solid solubility in Mg alloys at the eutectic temperature. A solid solution of Sn improves the electrode potential of the Mg matrix to improve the corrosion resistance. A previous report on Mg-1Sn alloy indicated favorable *in vitro* biocompatibility [37]. Tin is an n-type semiconductor material with a bandgap of approximately 3.6 eV in the form of SnO_2. It has high thermal stability and high transmittance in the IR and visible regions. It is often used for functional materials such as conductive electrodes in solar cells, flat panel displays, and gas sensors [38]. In addition, the addition of Sn to Mg alloys improves the mechanical properties due to solid solution strengthening [39]. The addition of Sn thus plays a dual role in the comprehensive properties of Mg alloys [40]. Mg_2Sn phases precipitated in Mg-xSn alloys promoted passivity but notably functioned as pitting corrosion initiation sites, while the solid solution Sn decreased the H_2 evolution rate [41]. According to Mg-Sn binary phase diagram, solid solubility of Sn in the Mg substrate significantly from 14.85 wt.% of the eutectic temperature dropped to 0.45 wt.% of 200 °C [42]. The addition of Sn was reported to have improved the mechanical properties of Mg-1Zn alloy due to the formation of the high melting point intermetallic compound of Mg_2Sn [42]. Moreover, Sn has mild antibacterial properties in the nanoscale regime [43,44]. Thus, to enhance the antibacterial behavior, Sn is often used to protect underwater optical instruments against the formation of biofilms in seawater [38]. Therefore, the content of Sn addition should limit to a relatively low lever to avoid excessive formation of Mg_2Sn phase. Based on the hope that the alloy has better corrosion resistance, the Sn content designed for Mg-1Zn alloy was selected to be 0.5% wt.

What is more, a study [45] showed that Mg metal has an effect on the colony forming units (CFUs) of both Gram-negative and Gram-positive bacteria, similar to the effect of a bactericidal fluoroquinolone antibiotic (enrofloxacin). Further, the results revealed that Mg corrosion products inhibit the growth of *E. coli, P. aeruginosa* and *S. aureus*. Zinc (II) ions can form strong bonds with the thiole, imidazole, amino and carboxyl groups of the microorganism membrane proteins of *S. aureus* bacteria, inducing structural changes to the membranes, consequently disturbing nutrient/protein transport and causing bacteria death [46]. Another study indicated that Zn can bind to bacterial DNA, otherwise inhibiting replication or inactivation of bacterial protein [47–49]. At the same time, the high pH environment produced during the degradation of magnesium alloys can inhibit a variety of bacteria. Based on the above reports, we hope to evaluate the antibacterial ability of the degradation products in the process of evaluating the degradation of the material *in vitro* to verify the potential antibacterial performance of the material.

However, a study on the corrosion behavior, biosafety and antibacterial properties of Mg-1Zn alloys with Sn could not be found in the literature. Hence, in the current study, the mechanical properties of Mg-4Zn-0.5Sn alloy were evaluated in detail, the *in vitro* and *in vivo* corrosion behavior, biosafety and the antibacterial ability brought about by its degradation, in order to develop an economical new orthopedic implant antibacterial magnesium alloy.

2. Materials and methods

2.1. Materials synthesis and characterization

2.1.1. Material preparation

High-purity Mg (99.98 wt.%), Zn (99.99 wt.%) and Sn (99.99 wt.%) in specific proportions were melted in an induction furnace under Ar gas protection. The prepared Mg-1Zn-0.5Sn alloy ingots measuring 80 mm in diameter were then extruded into bars with a length-to-width ratio of 25 at a temperature of 300 °C. The samples for investigation were cut from the extruded bars and successively ground to 1400 grit by SiC paper, ultrasonically cleaned in deionized water and ethanol and dried in cold air. Three replicates were prepared to evaluate the reproducibility of each test.

2.1.2. Microstructure characterization, mechanical properties, and degradation properties

The polished samples were etched by a solution of 2 ml of saturated picric acid and acetic acid and 8 ml of ethanol for microstructure observation [50]. The microstructure was examined by X-ray diffraction (XRD, Rigaku D/MAX-2500 PC) with Cu Kα radiation and scanning electron microscopy (SEM, VegaIILMU) with energy dispersive X-ray spectrometry (EDS) capability.

Extruded rods with a diameter of 16 mm were machined to dimensions of 2 mm in gauge thickness, 5 mm in gauge width and 10 mm in gauge length for tensile tests. Compression samples with diameters of 5 mm and heights of 10 mm were also prepared. Tension and compression tests were carried out on a SANS CMT5105 (CMS Co., Shenzhen, China) testing machine with a strain rate of 10–3 s^{-1} and 1 mm min^{-1}, respectively, at room temperature.

Electrochemical measurement at 37 °C in phosphate buffer solution (PBS) is an effective way to evaluate the *in vitro* degradation behavior. Samples mounted in self-curing denture acrylic with an exposed area of 0.785 cm^2 (φ10 mm) were used as working electrodes in a three-electrode system with a platinum plate as the counter electrode and a saturated calomel electrode (SCE) as the reference electrode. Before the measurements, 30 min of open-circuit potential was measured to establish a relatively stable state of the system. A potentiodynamic polarization curve was fitted by CorrView software, and a Nyquist plot from an electrochemical impedance spectroscopy (EIS) test was fitted by ZView software [51].

The immersion tests aimed mainly to obtain the corrosion rates through the hydrogen evolution volume and weight-loss method, which were performed at 37 °C in PBS following ASTM-G31-72 [52]. Samples of dimensions $10 \times 10 \times 7\ mm^3$ were immersed in a solution with a ratio of 20 mL/cm^2 (solution volume/surface area). Hydrogen was gathered in an inverted funnel and monitored by a scaled burette. Then, the immersion solution of each group at different time points (1, 3, 5, and 7 days) was sampled and sent to the magnesium alloy center of Chongqing University for ICP detection (Mg, Zn, and Sn). The results were normalized to the PBS results.

2.1.3. Hydrophilic testing

The hydrophilic properties of Mg-1Zn-0.5Sn composites were studied by the sessile drop method; Mg-1 Zn and titanium alloy were used as a control group. Distilled water was used as the media. A drop of distilled water was dropped onto the surface of each material, and the static contact angle was measured with a goniometer (Model 590; Ramé-hart, Succasunna, NJ, USA) at room temperature.

2.2. Antibacterial

2.2.1. Bacterial culture conditions and antibacterial test

E. coli O157: H7 NTCC: 12900 and S. aureus ATCC: 25923 were used as standard Gram-negative and Gram-positive strains for antibacterial studies, respectively. First, 100 μL of each bacterial suspension with a final concentration of 105 CFU mL^{-1} was transferred to 400 μL of leaching solution culture medium. Then, 150 μL of each inoculum suspension was plated in triplicate in a 96-well microtiter plate and incubated at 37 °C on a reciprocal shaker (120 rpm). The growth of the cultures was monitored every 2 h by measuring the optical density (OD) at 630 nm. All the experiments were performed in triplicate.

The antibacterial activity of the Mg-1Zn-0.5Sn materials was evaluated with the Gram-positive bacteria, S. aureus. The materials were incubated in MBH media with vigorous agitation until the optical density of the culture was 0.8 (absorbance) at 600 nm. The bacterial suspension was prepared by diluting the culture 10-fold with PBS. The Ti and Mg-1Zn material samples and glass as a control were cut into pieces measuring $1 \times 1\ cm^2$ and placed in Petri dishes. Then, 50 FL of diluted culture was dropped onto the surface of each film, and the dishes were incubated at room temperature. After incubation for the specific contact time, 5 ml of PBS was added to each dish, and the solution was gently mixed. Then, 100 μl of diluted suspension was taken out and immediately spread on MBH agar plates. These plates were incubated at 37 °C for 12 h, and the bacteria colonies were then counted.

2.2.2. Intracellular reactive oxygen species assay

To evaluate the intracellular reactive oxygen species (ROS) levels of bacterial cells on different samples, 2′, 7′-dichlorofluorescein diacetate (DCF) was used according to an established procedure. Briefly, bacteria (1 mL, 106 CFU/mL) were cultured with the samples at 37 °C for 24 h. Subsequently, 0.5 mL of DCF (10 μM) was added to each well and incubated for 30 min in an incubator. Next, 100 μL of this solution was transferred into a new 96-well plate. The fluorescence intensity (FI) of the DCF for each sample was detected with a microplate spectrophotometer (with an extinction wavelength at 488 nm and an emission wavelength at 535 nm). Finally, the DCF FI value, indicating the ROS level, was normalized against that of bacteria incubated on the Ti sample, and the final result was expressed as a change in the ROS concentration.

2.2.3. ATP level assessment

The ALP levels of bacteria adhered to different samples were measured. Briefly, 1 mL of bacterial suspension (1×106 CFU/mL) was grown on each sample substrate at 37 °C for 6 h. Then, the ATP levels of the suspensions were measured via the Enhanced ATP Assay Kit (Beyotime, China) with the luminescence intensity method.

2.3. Biocompatibility in vitro

2.3.1. Cytotoxicity assays

Dulbecco's modified Eagle's medium/nutrient mixture F-12 (DMEM/F12) with 10% fetal bovine serum was used as an extraction medium. An extraction solution of Mg-1Zn-0.5Sn and Mg-1Zn was used for comparison. The Cell Counting Kit-8 (CCK-8; Beyotime, Jiangsu, China) was used to investigate cell viability. Then, 200 μL of cell suspension was seeded into each well of a 96-well plate. Each well contained 2×104 viable cells per cm^2. On days 1, 3, and 5, 20 μL of CCK-8 solution was added to each well, and the plates were then incubated for 1 h. The plates were then read (in terms of the sample absorbance) at 450 nm using a microplate reader (Thermo Fisher Scientific Co Ltd, Waltham, MA, USA).

The survival activity of BMSCs grown on the sample was evaluated by live/dead staining. After being incubated for 1 day, the BMSCs (at an initial density of 2×104 cells/cm^2) were washed with PBS three times. Then, 1 mL of PBS containing 1 mM FDA and 2 mM PI was added to each well for staining. Subsequently, the treated BMSCs were cultured at 37 °C for 10 min and immediately visualized with fluorescence microscopy (Leica AF6000, Germany). The obtained images were used to quantify the dead cell number via IPP 6.0.

2.3.2. Lactate dehydrogenase (LDH) assay

The BMSCs were seeded onto samples at an initial density of 1×104 cells/cm^2. After culturing for 3 days, the culture media was collected, and the LDH activity was measured with an LDH assay kit at $\lambda = 490$ nm via a spectrophotometric microplate reader (Bio-Rad 680, USA).

2.3.3. Cell attachment and spreading

In this experiment, $1\,cm \times 1\,cm \times 0.1\,cm$ specimens of the different materials were prepared. BMSCs were cultured with different groups (glass control, Mg-1 Zn, and Mg-1Zn-0.5Sn) on a 24-well plate for 24 h. The cell density in each well was calculated to be approximately 3×104 cells/cm^2 using cell counting plates.

The cells were fixed in 4% paraformaldehyde for 15 min, Triton X-100 was added as a detergent, and the cells were stained with phalloidin (50 μg/mL; Cyagen, Guangzhou, China) for 30 min and then washed. Next, the cells were stained with 4′,6-diamidino-2-phenylindole (0.1 mg/mL; Cyagen, Guangzhou, China) for 15 min and imaged using CLS (Nikon, Tokyo, Japan). Finally, the cytoskeleton morphology was examined using inverted fluorescence microscopy (Leica SP8, Wetzlar, Germany) and ImageJ software. The cellular F-actin was characterized in terms of the aspect ratio and number of cells branching points. To evaluate the deformation, cell roundness was measured using the Image-Pro-Plus software (Media Cybernetics, Inc., USA). The cell roundness was expressed as the ratio of the average radius of curvature of the edge or corners to the radius of curvature of the maximum inscribed circle [12].

Table 1
Primer sequences for each gene.

Gene	5′−3′ sequence
GAPDH	F: 5′- GGCAAGTTCAACGGCACAGT-3′
	R: 5′- GCCAGTAGACTCCACGACAT-3′
Integrin	F: 5′- AGCTGGACATAGTCATCGTC-3′
$\alpha 1$	R: 5′- AGTTGTCATGCGATTCTCCG-3′
Integrin	F: 5′- AATGTTTCAGTGCAGAGCC-3′
$\beta 1$	R: 5′-TTGGGATGATGTCGGGAC −3′

2.3.4. Quantitative real-time polymerase chain reaction assay

BMSCs were cocultured with small disks of Mg-1 Zn, Mg-1Zn-0.5Sn and a glass control with diameters of 3 cm and thicknesses of 0.5 cm in a 6-well plate. DMEM-F12 was added to the cultured BMSCs, and the cell-attachment-related genes (integrin $\alpha 1$ and integrin $\beta 1$) were detected. The first established detection time point was 1 day after coculture with the samples. RNA was extracted using a total RNA kit (Omega Bio-Tek, Norcross, GA, USA) at each experimental time point. Complementary DNA was synthesized (at 37 °C for 15 min and 85 °C for 5 s) using a PrimeScript RT reagent kit (Takara, Shiga, Japan). A quantitative reverse transcription-polymerase chain reaction (qRT-PCR) assay was performed using the SYBR premix Ex Taq reagent (Takara) with a CFX Connect Real-Time PCR Detection System (Bio-Rad, Hercules, CA, USA). Primers were designed and synthesized by Sangon Biotech Co. Ltd. (Shanghai, People's Republic of China) using Primer Premier software (PREMIER Biosoft, Palo Alto, CA, USA). The primer sequences are presented in Table 1. Glyceraldehyde-3-phosphate dehydrogenase was used as an internal control. The relative expression of the target gene was calculated using the $2-\Delta\Delta Ct$ method according to the Ct values measured in previous reports.

2.4. Biosafety in vivo

2.4.1. Animal model

Four-week-old female Sprague–Dawley rats each weighing 200–240 g were obtained from the Laboratory Animal Center at Chongqing Medical University. The protocol was approved by the Ethics Committee of the First Affiliated Hospital of Chongqing Medical University Reference (IACUC No.: 2016-059). The rats were randomly divided into two groups of twelve animals such that there were at least six animals for each group at each time point. The rats were anesthetized using chloral hydrate (10%, 5.0–7.5 mL/kg), the left distal femoral condyle of each rat was exposed, and a bone defect with a diameter of 1.5 mm was created. Mg-1Zn-0.5Sn or Mg-1 Zn was inserted into the defects. After surgery completion,

penicillin was injected to prevent infection. After 1, 7, or 14 days feeding in the Laboratory Animal Center, the rats were euthanized using CO_2.

2.4.2. Biochemical analysis

Blood samples were collected by intracardiac puncture, and plasma was prepared by two successive centrifugations at $382 \times g$ (2000 rpm) for 20 min. Samples were stored at −20 °C until analysis by the First Affiliated Hospital of Chongqing Medical University. Alanine aminotransferase (ALAT), aspartate aminotransferase (ASAT) and creatinine plasmatic levels were quantified using an AU400 Chemistry Analyzer (Beckman Coulter). Interleukin-6 (IL-6) plasma levels were quantified by immunoassay using the Mouse Cytokine/Chemokine Magnetic Bead Panel (IL-6) (MCYTOMAG-70k, Millipore).

2.4.3. Histological analysis

Organs were carefully collected, fixed and conserved in formalin solution before paraffin embedding. Three-μm-thick paraffin sections of different organs were then processed manually. Slides were deparaffinized in three successive baths of xylene (Hydroclear) for 10 min and then rehydrated twice with 100% ethanol. After rising in tap water for 10 min, the slides were stained with Gründwald Hematoxylin for 30 s. After washing, the slides were stained with eosin for 15 s and rapidly rinsed in tap water and three baths of 100% ethanol. The slides were then stained in alcoholic safranin solution for 30 s, cleaned in xylene three times and mounted with Eukitt medium. The stained slides were scanned on a whole slide scanner (Nanozoomer 2.0-HT, Hamamatsu, Japan) at 40× magnification, and the obtained images were analyzed using NP-Viewer software.

3. Statistical analysis

Based on the normal distribution and equal variance assumption test, the data were expressed as the mean ± standard deviation and analyzed via one-way analysis of variance (ANOVA) with the Student Newman–Keuls (SNK) post hoc test. Statistical analysis was performed using SPSS 17.0 software. The differences were considered statistically significant at $p < 0.05$ (∗) and $p < 0.01$ (∗∗).

4. Results and discussion

4.1. Microstructure, mechanical properties, and in vitro *degradation*

Fig. 1a, b shows SEM-backscattered electron images of the extruded Mg-1Zn-0.5Sn alloys. The alloys exhibit an α-Mg solid solution with different quantities of small white dispersed particles. It is confirmed that there is no Sn-containing ternary phase formed in the Mg-Zn-Sn alloy system [53]. The formation of the intermetallic is related to the electronegative difference between different elements. Therefore, the Mg_2Sn phase forms preferentially in Mg-Zn-0.5Sn alloy because of the large electronegativity difference between Mg and Sn. Fig. 1c shows the XRD results of the investigated alloys. The Mg-1 Zn alloy is composed of α-Mg and dispersed impurities, while the Sn-containing alloys consist of α-Mg and a dispersed Mg_2Sn phase, combined with some impurities. According to the Mg-Sn phase diagram, Sn could be enriched in the liquid ahead of the solidification front, causing a constitutional super cooling zone of solid/liquid interface [42]. MgZn2 precipitates were thought to be nucleation sites for the Mg_2Sn precipitates [53]. This similar point was found in Ref [54]. also, the atom of Zn segregation at the interphase boundary facilitated the formation of Mg_2Sn phase. It can well illustrate the white particles B and C in Fig. 1 contains Zn and Sn together. The tensile YS is obviously enhanced by the addition of Sn into Mg-4 Zn alloy can be attributed to the solid solution strengthening and dispersion strengthening of Znrich particles (such as MgZn2) and Mg_2Sn particles

Table 2
Mechanical properties of Mg-Zn-0.5Sn.

Alloy	YS(MPa)	UTS(MPa)	Refs.
cortical bone	105–114	35–283	[55–57]
AZ31 extruded	185	264	
Mg-1Zn	110±3	211±11	
Mg-1Zn-0.5Sn	115±3	239±10	

The tensile stress-strain curves (Fig. 1d) demonstrate advantageous mechanical properties of the current alloys compared to Mg-1 Zn. Notably, 0.5Sn addition results in improvement in the strength and elongation. The phase composition as characterized by XRD shows that the Mg_2Sn phase is the only additional phase present. The mechanical parameters of present alloys, natural bone [55] and some Mg alloys [56,57] were summarized in Table 1. The yield strength (YS) and ultimate tensile strength (UTS) of Mg-1 Zn alloy are improved with Sn. The YS and UTS of all the investigated alloys exceed 100 MPa and 200 MPa, respectively, which means that extruded Mg-4ZnxSn alloys are available to meet the requirements of above 200 MPa for bone implant materials (Table 2), which was proposed by Erinc [58].

Fig. 1e shows potentiodynamic polarization curves of the studied alloys. The Sn-containing alloys exhibit higher cathodic current densities but lower anodic current densities than the Sn-free alloy. With Sn addition, the increasing amount of the second phase leads to additional cathodic hydrogen evolution sites. Therefore, the cathodic current density of the Sn-containing alloys is higher than that of the Sn-free Mg-1Zn alloy. However, the cathodic currents of all of the alloys are approximately the same because the high hydrogen evolution overvoltage of Sn can suppress hydrogen evolution to some degree [59]. As for the anodic branch, the alloys have a passivation tendency below the breakdown potential (Eb), indicating that protective films form on the surfaces. Hydrogen produced by the rapid degradation of magnesium alloys in the early post-implantation period is a key reason for limiting their use in medicine. Fig. 1f shows the hydrogen evolution with immersion time. The results reveal that

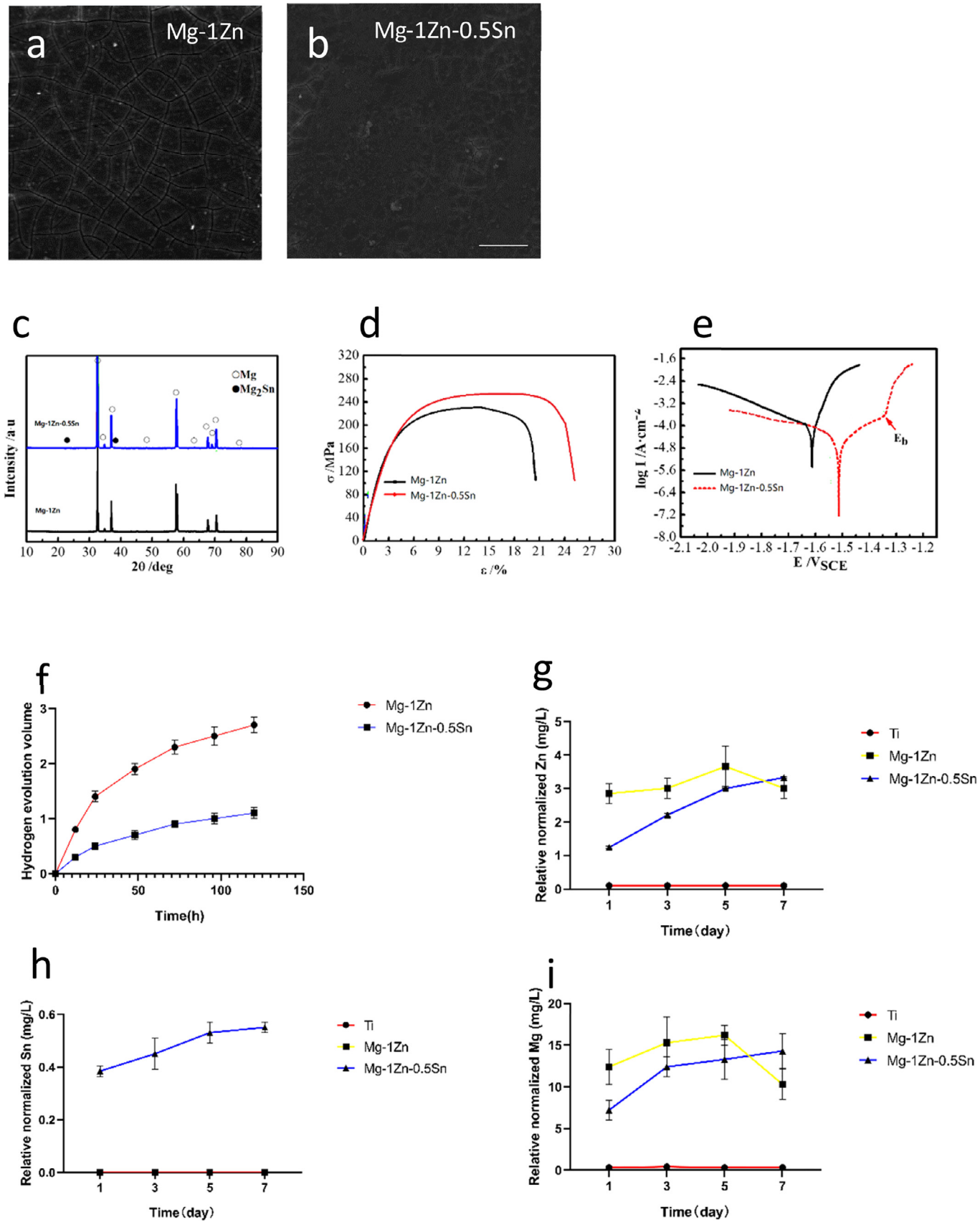

Fig. 1. Microstructures of the alloys (a) Mg-1 Zn and (b) Mg-1Zn-0.5Sn; (c) XRD patterns, (d) mechanical properties, and (e) potentiodynamic curves of the alloys. (f) hydrogen evolution volume of the alloys; ICP detection of the alloys (g) Zn, (h) Sn and (i) Mg. scale bar: 20 μm.

when Sn is added, the hydrogen evolution rate (VH) (by the equation pH = 2.279VH [60]) of Mg-1Zn-0.5Sn alloy is significantly lower than that of Mg-1Zn. The ICP results support this conclusion. After immersion in medium for 7 days, the amounts of released Zn and Mg are not significantly different. However, the amount of Mg-1Zn released over 24 h is significantly higher than that of the Mg-1Zn-0.5Sn group. It can be concluded that the use of Mg-1Zn-0.5Sn can reduce the rapid degradation rate significantly within 24 h compared to the Mg-1Zn group (Fig. 1g-i).

Bio-corrosion mechanism Indicated by the above studies, the Mg-1Zn-0.5Sn alloys showed decreased corrosion rate than Mg-1Zn alloy in PBS. Based on the results of the corrosion tests, the main chemical reactions may occur as follows:

$$MO + H_2O \rightarrow M\ (OH)_{(2)}\ (M = Mg,\ Zn) \quad (1)$$

$$M + 2H_2O \rightarrow M_2{}^{+} + 2OH^{-} + H_2\ (M = Mg,\ Zn) \quad (2)$$

$$M_2{}^{+} + 2H_2O^{-} \rightarrow M\ (OH)_2\ (M = Mg,\ Zn) \quad (3)$$

$$3M_2{}^{+} + 2PO_{3\text{-}4} \rightarrow M_3\ (PO_4)_2\ (M = Mg) \quad (4)$$

$$Sn\ H_4 + 2H_2O \rightarrow SnO_2 + 3H_2 \quad (5)$$

Oxidation usually happens when the samples are exposed in the air. Once the samples are immersed in PBS, the outer oxide layer would be converted into hydroxide contained layer (Eq. (1)). With time passing, the hydroxides continue to be attacked by corrosive Cl- and transform into soluble metallic ions and OH-. For Mg-1Zn-0.5Sn alloys, SnO/SnO_2 formed in the outer layer is stable and insoluble to water, isolating the alloys from solution. This may be one of the corrosion resistance mechanisms of Mg-1Zn-0.5Sn

When the solution penetrates through the outer layer to react with Mg matrix in the sequence of Mg and Zn (Eq. (2)), according to the aqueous half-cell potentials [61]. The reactions turn some elements in the substrate surface into metallic ions, increase the localized pH value. Then, solution will accumulate at the bottom of these holes, and continue to destroy the holes, accompanied by the destructive effect of the evolution of H_2. Differently, for Mg-1Zn-0.5Sn alloys, Mg_2Sn phases acts as initiation sites of galvanic corrosion, and Mg areas adjacent to Mg_2Sn phases preferentially dissolve into metallic ions with some hydrogen evolved, which also leads to local alkalization. Meanwhile, the rapid increase of pH value leads to the precipitation of the insoluble hydroxides $Zn(OH)_2$ and $Mg(OH)_2$ (Eq. (3)), as the solubility products (Ksp) is $3.05 \times 10{-}16$ and $1.8 \times 10{-}11$ [44], respectively. These precipitates could slow down the corrosion process by filling up and repairing the pitting holes. As the corrosion proceeds, phosphate will also be formed and precipitated on the surface continuously (Eq. (4)). However, since Cl-can react with hydroxides to form chloride, the precipitants are insufficient to protect the Mg matrix for Mg-1 Zn alloy. According to the Pourbaix E-pH diagram of Sn-H_2O [62], tin hydride (SnH_4) might form firstly. SnH_4 was reported to react with water to form SnO_2 (Eq. (5)) [63]. Therefore, this dense SnO_2 in Sn-bearing Mg-1 Zn alloys, incorporated in the surface film, offers strong protectiveness to pitting corrosion.

4.2. Cell proliferation and attachment

The initial adhesion, morphology, and viability of BMSCs were characterized to investigate the cytocompatibility of the material samples *in vitro*. After 1 day of culturing, the number of BMSCs in the Mg-1 Zn group decreased significantly (Fig. 2a) relative to other groups. This may be due to the rapid degradation of Mg-1 Zn, which rapidly increases the pH value and affects the adhesion and proliferation of BMSCs. It is notable that the number of BMSCs on Mg-1Zn-0.5Sn and Ti exhibited no difference after culturing for 1 day, indicating that the degradation of Mg-1Zn-0.5Sn samples does not disrupt BMSC adhesion. Fig. S1 presents the water contact angles of the Mg-1Zn, Mg-1Zn-0.5Sn, and Ti. These results indicate that the hydrophilicity of the Mg-1Zn-0.5Sn composites is better than those of Ti and Mg-1 Zn and that Mg-1Zn-0.5Sn is more biocompatible than the other materials. A difference was observed after culturing for 3 days; BMSCs in the Mg-1Zn-0.5Sn group exhibited significantly higher proliferation ability than other groups, indicating that products from the degradation of Mg-1Zn-0.5Sn samples could have a positive effect on proliferation (Fig. 2a). Furthermore, a similar tendency in the Mg-1 Zn group was observed with culture times of 5 and 7 days. It can be concluded that as the degradation of Mg-1 Zn slows down, the pH decreases, and the accumulation of Mg and Zn plays a role in promoting BMSC proliferation ($p < 0.05$). As shown by the PCR results (Fig. 2b,c), the gene expression of integrins $\alpha 1$ and $\beta 1$ in the Mg-1 Zn group was significantly lower than that in the other groups at the 1-day time point ($p < 0.05$). However, at the 3- and 5-day time points, the integrin ($\alpha 1$ and $\beta 1$) expression of this group was significantly increased (compared to the Ti group). Although the Mg-1Zn-0.5Sn results were not significantly different from the control group results on the first day, the expression at the other time points was significantly increased over that of the other groups. After the rapid degradation period (24 h), the Mg and Zn ions and relatively high pH values produced by slowly degrading Mg alloys were found to be beneficial for BMSCs to express integrins $\alpha 1$ and $\beta 1$ [64]. In addition, the morphologies of the BMSCs were observed with cytoskeleton staining after culturing for 24 h (Fig. 2d). The BMSCs on Ti presented a spreading morphology with a fusiform shape. In comparison, BMSCs spread more, with protruding pseudopodia, on Mg-1Zn-0.5Sn. BMSCs cultured on Mg-1Zn-0.5Sn exhibited more pseudopodia than those of other groups, indicating that the ions released through degradation and the hydrophilic surfaces enhanced BMSC attachment and spreading. In addition, the results of the LDH assay indicated that the obtained Mg-1Zn-0.5Sn group presented no detectable cytotoxicity to BMSCs (Fig. S2). Cytoskeletal staining and roundness statistics were used to evaluate the molecular arrangement and concentration and occurrence of cell deformation on the surfaces of the various materials after culturing

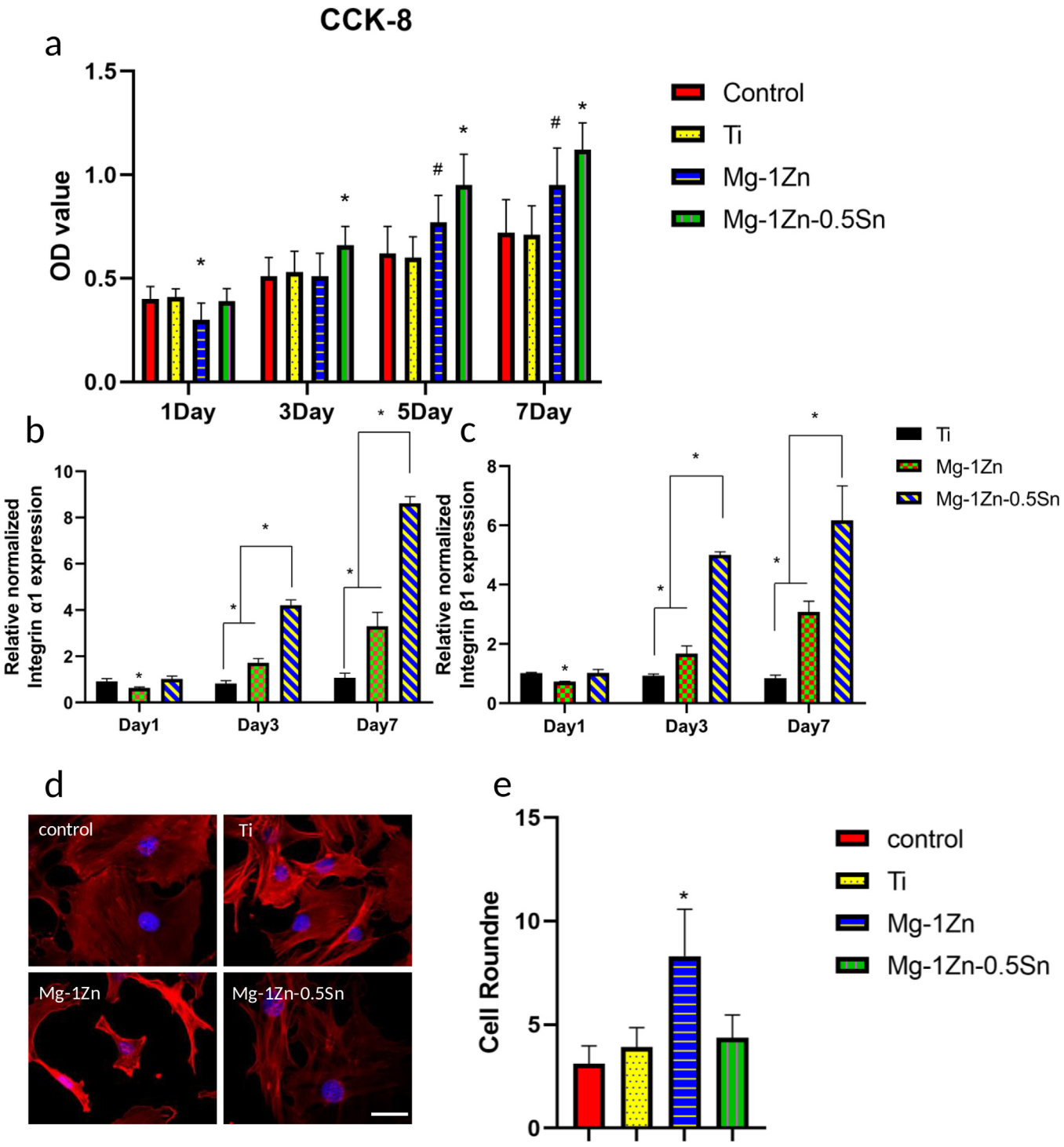

Fig. 2. (a) Cell viability of BMSCs evaluated with the CCK-8 assay. Error bars represent the mean ± SD ($n=6$), * compared to other groups, # compared to Ti and the control group ($p < 0.05$). Relative mRNA expression of cell attachment genes: (b) integrin $\alpha 1$ and (c) integrin $\beta 1$ of BMSCs grown on various substrates after culturing for 1 day; β-actin was used as a control. Error bars represent the mean ± SD for $n=3$ ($^*p < 0.05$); (d) initial BMSC adhesion on various material substrates and the cytoskeleton staining of BMSCs of different groups. Cell nuclei stained with DAPI (blue) and cells stained with phalloidin (red) after culturing for 24 h. (e) Calculated roundness of cells; error bars represent mean ± SD for $n=30$ ($^*p < 0.05$). scale bar: 50 μm.

for 24 h. Compared with the results of the control group, the cell roundness in the Mg-1 Zn groups was increased by 58%. These results suggest that the Mg-1 Zn induces deformation. However, the cell roundness in the Mg-1Zn-0.5Sn groups was decreased slightly by 12% (Fig. 2e). As a result, Mg-1Zn-0.5Sn is concluded to provide better biocompatibility than the other materials, consistent with the live/dead staining results (Figs. S3,S4). Nevertheless, the viability of BMSCs cultured on Mg-1Zn-0.5Sn was higher ($p < 0.01$) than that of Ti and Mg-1 Zn. Remarkably, a similar trend was observed for a culture time of 7 days. The release profiles of Mg, Zn, and Sn from the Mg-1 Zn and Mg-1Zn-0.5Sn samples were measured with ICP. The release rate of Mg-1Zn-0.5Sn in PBS was slower than that of Mg-1 Zn, indicating that Sn decreases the rapid release of alloy constitutive metals. A similar result was observed when the Mg-1 Zn and Mg-1Zn-0.5Sn samples were exposed to DMEM/F12 with a pH value of 7.9 (Fig. S5). The degradation process of Mg-1Zn-0.5Sn was slower than that of the Mg-1 Zn group. This result indicates not only that the mechanical properties of Mg-1Zn-0.5Sn can be maintained long after implantation in the human body but also that the new material can reduce the deleterious side effects (involving excessive OH- and H_2 production) of Mg alloy implantation.

4.3. Alkalinity evaluation and antibacterial activity

It has been reported that the alkaline microenvironment surrounding biodegradable implants not only improves BMSC viability but also inhibits bacterial growth *in vitro* and *in vivo*, both of which benefit bone repair [65,66]. In addition, microenvironments with high pH values (<8.0) can lead to bacterial death, enhancing the antimicrobial property of implants and benefiting the repair of infected bone [67]. Hence, the alkalinity of each sample with bacteria (E. coli and S. aureus) and BMSCs merits investigation. It was found that the pH of an MBH medium culture of E. coli and S. aureus sharply decreased within 24 h, while the pH of a DMEM/F12 culture of BMSCs slightly decreased from 7.9 to 7.6 (Fig. S5). Furthermore, both E. coli and S. aureus on Ti produced acidic environments and led to significant reductions in pH values. Specifically, the relative pH values of the Ti groups were approximately 6.1 for E. coli and approximately 5.2 for S. aureus (Figs. S6, S7).

However, in all Mg alloy materials, interface pH values were not impacted by bacteria but instead maintained microenvironmental alkalinity (pH > 7.8) over 24 h (Figs. S6, S7). In addition, the local pH of all samples with BMSCs did not exhibit an acidic microenvironment in DMEM/F12 medium. The degradation of Mg-1Zn-0.5Sn and Mg-1 Zn cultured with bacteria and BMSCs provided an appropriate alkaline microenvironment with a pH value exceeding 8. The antibacterial properties of the samples were then challenged with E. coli and S. aureus via the spread plate method, following previous studies [67,68]. As shown in Fig. 3a,b, the Mg-1 Zn group and the Mg-1Zn-0.5Sn group exhibited a significant reduction in the bacterial population in the coculture liquid at all detection time points compared with the Ti group. The results shown in Fig. 3c are consistent with this conclusion. The resulting colonies of E. coli and S. aureus on the Mg-1 Zn and Mg-1Zn-0.5Sn substrates were smaller than those on Ti. After sample degradation in DMEM or PBS medium, the pH change for each group was observed (Fig. S8). The results showed that although there was no significant difference in pH between the two groups after 120 h, the early pH of the Mg-1Zn-0.5Sn group was significantly lower than that of the Mg-1 Zn group. This slow pH elevation facilitates early cell adhesion while providing an alkaline environment comparable to that of the Mg-1 Zn group.

Furthermore, although the pH value of the Mg-1Zn-0.5Sn group was lower than that of Mg-1 Zn, the Mg-1Zn-0.5Sn group exhibited better bacterial ability. The antibacterial effect is therefore attributed to the presence of Sn. In a previous study, Zn^{2+} was found to correspond to one of the significant inorganic metal oxides exhibiting excellent antibacterial activities [69]. It has been recently well established that doping processes can improve the antibacterial efficacy of alloys. In particular, dopants such as Sn play a vital role in enhancing the antimicrobial activities of zinc alloy [37,70,71]. This might be the reason why the Mg-1Zn-0.5Sn group exhibited better antibacterial properties than the Mg-1 Zn group in the bacterial CFU test.

It has been confirmed that the antibacterial pathway of released Zn^{2+} is based on the production of ROS [27,72]. As shown in Fig. 3d, a measurement of the intracellular ROS levels of samples determined that the intracellular ROS levels gathered in E. coli from the Mg-1 Zn and Mg-1Zn-0.5Sn samples were higher ($p < 0.01$) than that of the Ti group. A similar phenomenon was observed for S. aureus. However, Sn might not play a role in antibacterial ROS. Under normal conditions, protons enter the cell through the proton channels to combine with existing F-type (H^+-transporting) ATPase and take part in the process of ATP production [73,74]. Thus, the bacteria are hindered, even to the point of death, due to the inhibition of ATP synthesis and the associated energy shortfall [75]. Fig. S9 shows that, compared to the Ti group, both Mg alloy groups decrease the ATP levels in bacteria, and the Mg-1Zn-0.5Sn group shows lower ATP levels than the Mg-1 Zn group, which means that Sn might inhibit bacteria in the manner described above.

In detail, the Mg alloy surface sustainably releases OH^- ions that continuously react with hydrogen ions from the bacterial extracellular environment and reduce the ATP level of bacteria [67]. Moreover, the level of bacterial intracellular ROS increases substantially due to the transformation of the alkaline microenvironment and the release of Zn^{2+}. Finally, the new antibacterial agent Sn inhibits the activity of bacterial proliferation.

4.4. In vivo *biosafety and biocompatibility*

This study also focused on *in vivo* biosafety and biocompatibility. With the degradation of magnesium alloy, H_2,

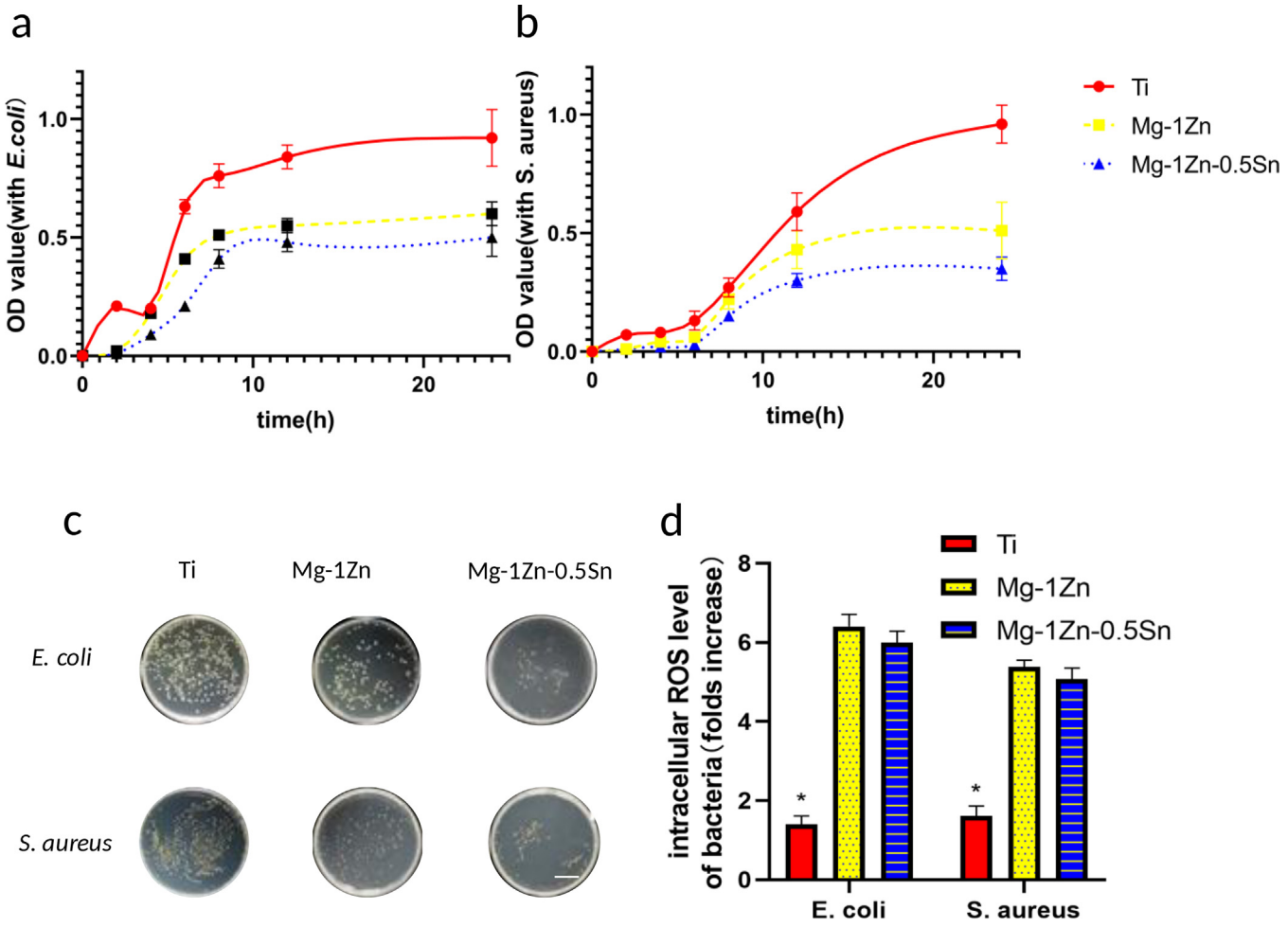

Fig. 3. (a) *E. coli* and (b) *S. aureus* inhibition results of bacteria suspension cocultured with leaching solution culture medium; (c) images of Petri dishes with *E. coli* and *S. aureus* cultivated on MBH agar covered with a bacteria suspension cocultured with different materials. (d) Intracellular ROS levels of *E. coli* and *S. aureus* cultured on different material substrates. Error bars represent mean±SD ($n=6$), $^{*}p < 0.05$. scale bar: 2 cm.

OH−, and free Mg ions, Zn ions and Sn ions are generated, which might cause damage to surrounding tissues or the whole body. First, to determine if the materials induced liver toxicity, we measured the plasma ASAT and ALAT contents. An increase in these enzymes is considered a key marker of hepatocellular injury. The ALAT and ASAT levels remained normal in Mg-1Zn-0.5Sn group animals for 14 days as compared to the control group with a mean value of approximately 201 U/L and 52 U/L for ASAT and ALAT, respectively (Fig. 4a, b). Although the ASAT level of Mg-1Zn-0.5Sn was significantly higher than that of other groups for 24 h, it had returned to a lower level at 7 days, indicating the absence of liver dysfunction. Kidney function was assessed by measuring the creatinine plasma level. We did not observe any significant difference between the Mg-1Zn-0.5Sn-treated groups sacrificed at any time points and the control group (Fig. 4c). Importantly, these values remained under the toxicity threshold and were consistent with literature reports of normal function (30 μmol/L) [76–78]. The potential inflammatory effect of Mg-1Zn-0.5Sn was determined by the plasma level of IL-6, a well-recognized mediator of inflammation. In the control group, the average level of IL-6 was approximately 30 pg/ml as described in the literature. Relative to the control group, the IL-6 level was not significantly modified at 24 h, 7 days or 14 days post-treatment (Fig. 4d). These results, combined with histological analysis, indicate that even if Mg, Sn, and Zn accumulate in the liver, they do not alter hepatic function.

These results confirm that, compared to Ti and the control group, Mg-1Zn-0.5Sn implantation is safe, inducing no acute or chronic toxicity or weight loss in the animals (Fig. 4e). Moreover, any increase in the IL-6 level was transitory, caused by surgery, and returned to a normal value one week later, suggesting the absence of additional inflammation. Combined, these results provide evidence that metal ion (Mg, Zn or Sn) accumulation in the liver and small amounts in the kidney due to alloy degradation do not affect organ functionality.

These results, in conjunction with histological analysis, indicate that even if Mg, Sn, and Zn accumulate in the liver, they do not alter hepatic, spleen or kidney structure (Fig. 4f).

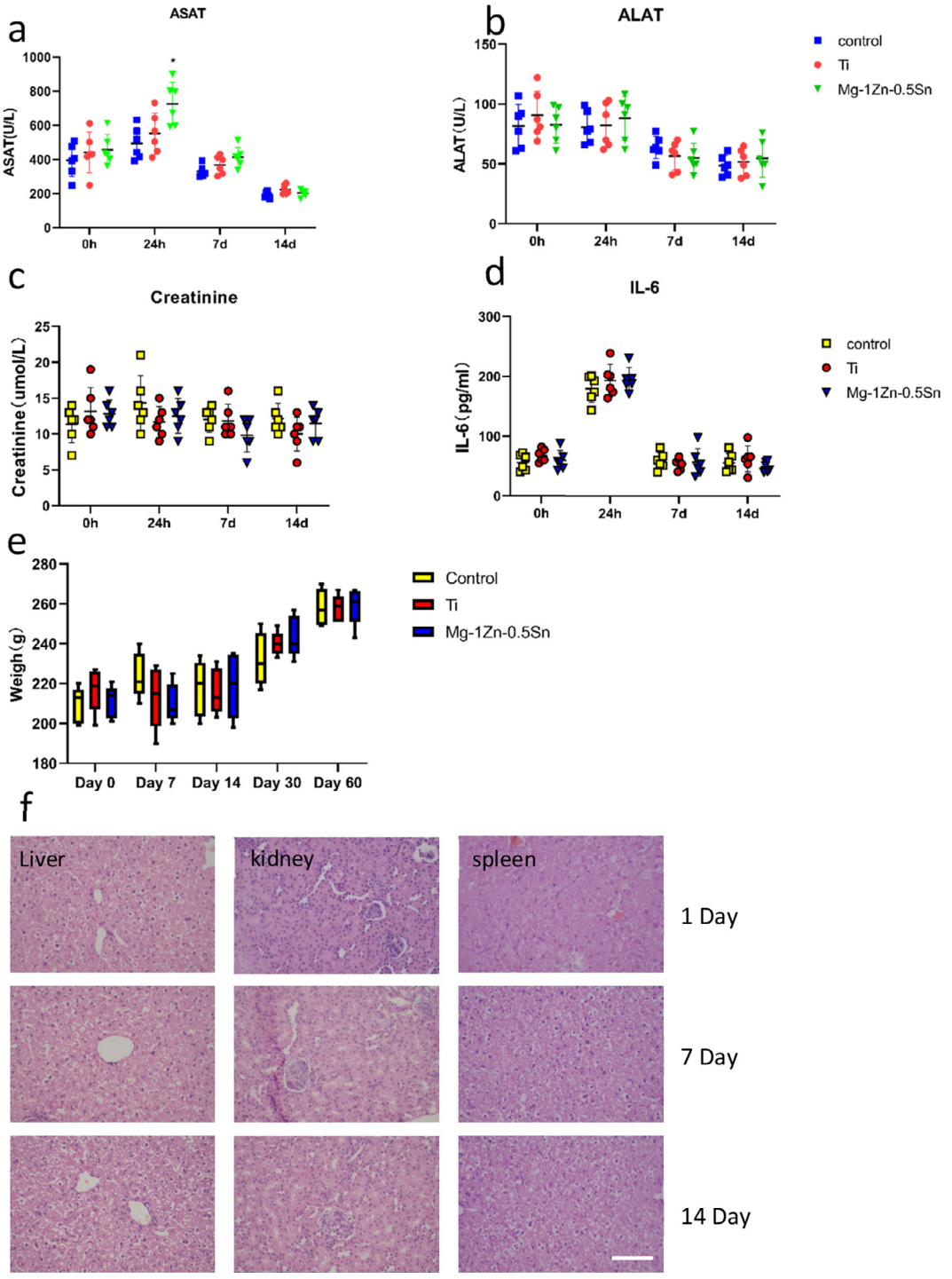

Fig. 4. (a) ASAT and (b) ALAT values, (c) creatinine level (d) and IL-6 concentration in rat plasma and (e) rat weight at 24 h or 7 or 14 days after implantation. Data represent the mean ± SEM of 6 rats, and statistical significance was identified ($^*p < 0.05$). (f) The 3D structure of Mg-1Zn-0.5Sn after material degradation *in vivo*. (g) H&E staining images of the major organs of Sprague–Dawley rat liver, spleen, and kidney in various groups, scale bar: 100 μm.

5. Conclusion

From this study, following research on the properties of the Mg alloy itself, its antibacterial properties, and its biocompatibility *in vitro* and *in vivo*, we can draw the following conclusions:

(1) The effects of Sn on the degradation and biocorrosion properties of as-extruded Mg-1 Zn alloys are investigated in this work. Due to solid solution strengthening, the mechanical properties are slightly improved by Sn addition. In addition, a small amount of Sn added to Mg-1 Zn alloy reduces the biocorrosion rate, which

might be attributed to Sn participation in the outer-layer film formation, which would reduce side effects such as hydrogen accumulation after implantation *in vivo*.

(2) Mg-1Zn-0.5Sn materials exhibited significant antibacterial ability compared to Ti materials. On the one hand, this is because the material provides an alkalized environment during the degradation process, which is not conducive to bacterial growth. On the other hand, the Mg and Zn ions and their degradation products produced by the degradation of the material have an additional antibacterial effect. Furthermore, Sn ions also play an important role in this antibacterial activity. It can be concluded that Mg-1Zn-0.5Sn has excellent antibacterial potential in medical applications.

(3) Compared with Mg-1 Zn, Mg-1Zn-0.5Sn has excellent biocompatibility. *In vitro*, BMSCs exhibited better adhesion, better proliferative capacity and lower mortality on the surface of Mg-1Zn-0.5Sn than on the other surfaces. Furthermore, Mg-1Zn-0.5Sn implantation did not cause liver or kidney toxicity and did not cause additional inflammatory reactions, in contrast to the traditional medical metal Ti. These collective results show that Mg-1Zn-0.5Sn has great potential as a medical material.

Supplementary materials

Supplementary material associated with this article can be found, in the online version, at doi:10.1016/j.jma.2020.02.008.

References

[1] N. Eliaz., Materials (Basel) 12 (3) (2019).
[2] S. Maietta, A. Gloria, G. Improta, M. Richetta, R. De Santis, M. Martorelli, J Healthc. Eng. 2019 (2019) 3212594.
[3] M. Janbozorgi, K.K. Taheri, A.K. Taheri, J. Magn. Alloys 7 (1) (2019) 80–89.
[4] A.R. Amini, J.S. Wallace, S.P. Nukavarapu, J. Long Term Eff. Med. Implants 21 (2) (2011) 93–122.
[5] C. Liu, Z. Ren, Y. Xu, S. Pang, X. Zhao, Y. Zhao, Biodegrad. Scan. 2018 (2018) 9216314.
[6] W.Y. Jiang, J.F. Wang, W.K. Zhao, Q.S. Liu, D.M. Jiang, S.F. Guo, J. Magn. Alloys 7 (1) (2019) 15–26.
[7] S. Ramesh, G. Anne, H.S. Nayaka, S. Sahu, M.R. Ramesh, J. Magn. Alloys 7 (3) (2019) 444–455.
[8] M. Carboneras, M.C. Garcia-Alonso, M.L. Escudero, Corros. Sci. 53 (4) (2011) 1433–1439.
[9] J. Sullivan, N. Cooze, C. Gallagher, T. Lewis, T. Prosek, D. Thierry, Faraday Discuss. 180 (2015) 361–379.
[10] Y. Jang, B. Collins, J. Sankar, Y. Yun, Acta Biomater. 9 (10) (2013) 8761–8770.
[11] M. Haghshenas, J. Magn. Alloys 5 (2) (2017) 189–201.
[12] G.L. Song, A. Atrens, Adv. Eng. Mater. 5 (12) (2003) 837–858.
[13] M. Razavi, M. Fathi, O. Savabi, D. Vashaee, L. Tayebi, J. Mater. Sci.-Mater. Med. 26 (5) (2015).
[14] M. Razavi, M. Fathi, O. Savabi, L. Tayebi, D. Vashaee, J. Mater. Sci.-Mater. Med. 29 (10) (2018).
[15] F. Witte, V. Kaese, H. Haferkamp, E. Switzer, A. Meyer-Lindenberg, C.J. Wirth, H. Windhagen, Biomaterials 26 (17) (2005) 3557–3563.
[16] G.L. Song, Corros. Sci. 49 (4) (2007) 1696–1701.
[17] B. Zberg, P.J. Uggowitzer, J.F. Loffler, Nat. Mater. 8 (11) (2009) 887–891.
[18] D.T. Chou, D. Hong, P. Saha, J. Ferrero, B. Lee, Z. Tan, Z. Dong, P.N. Kumta, Acta Biomater. 9 (10) (2013) 8518–8533.
[19] A. Smirnov, A. Seleznev, N.W. Solis Pinargote, Y. Pristinskiy, P. Peretyagin, J.F. Bartolome, Nanomaterials (Basel) 9 (10) (2019).
[20] M.S. Uddin, C. Hall, P. Murphy, Sci. Technol. Adv. Mater. 16 (5) (2015) 053501.
[21] N. Sezer, Z. Evis, S.M. Kayhan, A. Tahmasebifar, M. Koc, J. Magn. Alloys 6 (1) (2018) 23–43.
[22] A. Dubey, S. Jaiswal, D. Lahiri, J. Mater. Eng. Perform. 28 (2) (2019) 800–809.
[23] N. Sriraman, S. Kumaran, Mater. Res. Exp. 6 (5) (2019) 056524.
[24] C.H. Wang, Z.L. Yi, Y.F. Sheng, L. Tian, L. Qin, T. Ngai, W. Lin, Mater. Sci. Eng. C-Mater. Biol. Appl. 99 (2019) 344–356.
[25] M. Razavi, M. Fathi, O. Savabi, D. Vashaee, L. Tayebi, J. Biomed. Mater. Res. A 103 (5) (2015) 1798–1808.
[26] G.L. Xu, L.G. Zhang, L.B. Liu, Y. Du, F. Zhang, K. Xu, S.H. Liu, M.Y. Tan, Z.P. Jin, J. Magn. Alloys 4 (4) (2016) 249–264.
[27] X.K. Shen, Y. Hu, G.Q. Xu, W.Z. Chen, K. Xu, Q.C. Ran, P.P. Ma, Y.R. Zhang, J.H. Li, K.Y. Cai, ACS Appl. Mater. Interfaces 6 (18) (2014) 16426–16440.
[28] F. Rosalbino, S. De Negri, G. Scavino, A. Saccone, J. Biomed. Mater. Res. A 101 (3) (2013) 704–711.
[29] X. Tong, D. Zhang, X. Zhang, Y. Su, Z. Shi, K. Wang, J. Lin, Y. Li, J. Lin, C. Wen, Acta Biomater. 82 (2018) 197–204.
[30] E. Mostaed, M. Sikora-Jasinska, A. Mostaed, S. Loffredo, A.G. Demir, B. Previtali, D. Mantovani, R. Beanland, M. Vedani, J. Mech. Behav. Biomed. Mater. 60 (2016) 581–602.
[31] F.Y. Zhou, B.L. Wang, K.J. Qiu, L. Li, J.P. Lin, H.F. Li, Y.F. Zheng, J. Biomed. Mater. Res. B Appl. Biomater. 101 (2) (2013) 237–246.
[32] C. Zhao, F. Pan, S. Zhao, H. Pan, K. Song, A. Tang, Mater. Sci. Eng. C Mater. Biol. Appl. 54 (2015) 245–251.
[33] W. Sun, G. Zhang, L. Tan, K. Yang, H. Ai, Mater. Sci. Eng. C Mater. Biol. Appl. 63 (2016) 506–511.
[34] H.R. Bakhsheshi-Rad, E. Hamzah, M. Kasiri-Asgarani, S. Jabbarzare, N. Iqbal, M.R. Abdul Kadir, Mater. Sci. Eng. C Mater. Biol. Appl. 60 (2016) 526–537.
[35] V.K. Bommala, M.G. Krishna, C.I. Rao, J. Magn. Alloys 7 (1) (2019) 72–79.
[36] E. Zhang, S. Li, J. Ren, L. Zhang, Y. Han, Mater. Sci. Eng. C Mater. Biol. Appl. 69 (2016) 760–768.
[37] A. Sirelkhatim, S. Mahmud, A. Seeni, N.H.M. Kaus, L.C. Ann, S.K.M. Bakhori, H. Hasan, D. Mohamad, Nano-Micro Lett. 7 (3) (2015) 219–242.
[38] J. Henry, K. Mohanraj, G. Sivakumar, S. Umamaheswari, Spectrochim. Acta A Mol. Biomol. Spectrosc. 143 (2015) 172–178.
[39] R. Vink, Magnes. Res. 29 (3) (2016) 95–101.
[40] L. Lvova, C.G. Goncalves, C. Di Natale, A. Legin, D. Kirsanov, R. Paolesse, Talanta 179 (2018) 430–441.
[41] H.Y. Ha, J.Y. Kang, S.G. Kim, B. Kim, S.S. Park, C.D. Yim, B.S. You, Corros. Sci. 82 (2014) 369–379.
[42] S.H. Wei, T.P. Zhu, M. Hodgson, W. Gao, Mater. Sci. Eng.-Struct. Mater. Prop. Microstruct. Process. 585 (2013) 139–148.
[43] R.P. Senthilkumar, V. Bhuvaneshwari, R. Ranjithkumar, S. Sathiyavimal, V. Malayaman, B. Chandarshekar, Int. J. Biol. Macromol. 104 (Pt B) (2017) 1746–1752.
[44] K. Arunachalam, B. Shanmuganathan, P.S. Sreeja, T. Parimelazhagan, Environ. Sci. Pollut. Res. Int. 22 (22) (2015) 18066–18075.
[45] A. Perez-Anes, M. Gargouri, W. Laure, H. Van Den Berghe, E. Courcot, J. Sobocinski, N. Tabary, F. Chai, J.F. Blach, A. Addad, P. Woisel, D. Douroumis, B. Martel, N. Blanchemain, J. Lyskawa, ACS Appl. Mater. Interfaces 7 (23) (2015) 12882–12893.
[46] J. Yoo, A. Birke, J. Kim, Y. Jang, S.Y. Song, S. Ryu, B.S. Kim, B.G. Kim, M. Barz, K. Char, Biomacromolecules 19 (5) (2018) 1602–1613.
[47] A. Brauner, O. Fridman, O. Gefen, N.Q. Balaban, Nat. Rev. Microbiol. 14 (5) (2016) 320–330.

[48] J. Della Rocca, D. Liu, W. Lin, Acc. Chem. Res. 44 (10) (2011) 957–968.
[49] R. Banerjee, A. Phan, B. Wang, C. Knobler, H. Furukawa, M. O'Keeffe, O.M. Yaghi, Science 319 (5865) (2008) 939–943.
[50] Y. Jang, Z. Tan, C. Jurey, Z. Xu, Z. Dong, B. Collins, Y. Yun, J. Sankar, Mater. Sci. Eng. C Mater. Biol. Appl. 48 (2015) 28–40.
[51] J.Z. Chen, G.A. Li, X. Cai, J.T. Jiang, W.Z. Shao, L. Yang, L. Zhen, Materials (Basel) 11 (5) (2018).
[52] T.T. Sasaki, J.D. Ju, K. Hono, K.S. Shin, Scr. Mater. 61 (1) (2009) 80–83.
[53] C.Q. Liu, H.W. Chen, J.F. Nie, Scr. Mater. 123 (2016) 5–8.
[54] S.H. Wei, T.P. Zhu, H.B. Hou, J. Kim, E. Kobayashi, T. Sato, M. Hodgson, W. Gao, Mater. Sci. Eng.-Struct. Mater. Prop. Microstruct. Process. 597 (2014) 52–61.
[55] D. Hong, P. Saha, D.T. Chou, B. Lee, B.E. Collins, Z.Q. Tan, Z.Y. Dong, P.N. Kumta, Acta Biomater. 9 (10) (2013) 8534–8547.
[56] X.B. Zhang, G.Y. Yuan, L. Mao, J.L. Niu, W.J. Ding, Mater. Lett. 66 (1) (2012) 209–211.
[57] F. Witte, N. Hort, C. Vogt, S. Cohen, K.U. Kainer, R. Willumeit, F. Feyerabend, Curr. Opin. Solid State Mater. Sci. 12 (5–6) (2008) 63–72.
[58] M. Erinc, W.H. Sillekens, R.G.T.M. Mannens, R.J. Werkhoven, Magn. Technol. 2009 (2009) 209–214.
[59] S. Bouden, A. Dahi, F. Hauquier, H. Randriamahazaka, J. Ghilane, Sci. Rep. 6 (2016) 36708.
[60] L. Yang, E.L. Zhang, Mater. Sci. Eng. C-Biomim. Supramol. Syst. 29 (5) (2009) 1691–1696.
[61] T. Ohtsuka, A. Nishikata, M. Sakairi, K. Fushimi, Electrochem. Corros. Fundam. (2018) 1–15.
[62] X.B. Liu, D.Y. Shan, Y.W. Song, R.S. Chen, E.H. Han, Electrochim. Acta 56 (5) (2011) 2582–2590.
[63] J.F. Wang, Y. Li, S. Huang, X.E. Zhou, Appl. Surf. Sci. 317 (2014) 1143–1150.
[64] Y.Q. Yu, G.D. Jin, Y. Xue, D.H. Wang, X.Y. Liu, J. Sun, Acta Biomater. 49 (2017) 590–603.
[65] Y. Shen, W. Liu, K. Lin, H. Pan, B.W. Darvell, S. Peng, C. Wen, L. Deng, W.W. Lu, J. Chang, Langmuir 27 (6) (2011) 2701–2708.
[66] J. Liang, S. Xu, M. Shen, B. Cheng, Y. Li, X. Liu, D. Qin, A. Bellare, L. Kong, Int. J. Nanomed. 12 (2017) 1317–1328.
[67] J. Tan, D. Wang, H. Cao, Y. Qiao, H. Zhu, X. Liu, ACS Appl. Mater. Interfaces 10 (49) (2018) 42018–42029.
[68] W. Liu, T. Wang, C. Yang, B.W. Darvell, J. Wu, K. Lin, J. Chang, H. Pan, W.W. Lu, Osteoporos. Int. 27 (1) (2016) 93–104.
[69] O. Yamamoto, Int. J. Inorg. Mater. 3 (7) (2001) 643–646.
[70] J. Sawai, E. Kawada, F. Kanou, H. Igarashi, A. Hashimoto, T. Kokugan, M. Shimizu, J. Chem. Eng. Jpn. 29 (4) (1996) 627–633.
[71] K.R. Raghupathi, R.T. Koodali, A.C. Manna, Langmuir 27 (7) (2011) 4020–4028.
[72] C.Y. Mao, Y.M. Xiang, X.M. Liu, Z.D. Cui, X.J. Yang, K.W.K. Yeung, H.B. Pan, X.B. Wang, P.K. Chu, S.L. Wu, ACS Nano 11 (9) (2017) 9010–9021.
[73] J. Tan, D.H. Wang, H.L. Cao, Y.Q. Qiao, H.Q. Zhu, X.Y. Liu, ACS Appl. Mater. Interfaces 10 (49) (2018) 42018–42029.
[74] H.L. Cao, K.W. Tang, X.Y. Liu, Mater. Horiz. 5 (2) (2018) 264–267.
[75] L. Bai, Z.B. Du, J.J. Du, W. Yao, J.M. Zhang, Z.M. Weng, S. Liu, Y. Zhao, Y.L. Liu, X.Y. Zhang, X.B. Huang, X.H. Yao, R. Crawford, R.Q. Hang, D. Huang, B. Tang, Y. Xiao, Biomaterials 162 (2018) 154–169.
[76] Q.Q. Chen, Y. Xue, J. Sun, Int. J. Nanomed. 8 (2013) 1129–1140.
[77] T. Baati, A. Al-Kattan, M.A. Esteve, L. Njim, Y. Ryabchikov, F. Chaspoul, M. Hammami, M. Sentis, A.V. Kabashin, D. Braguer, Sci. Rep. 6 (2016) 1–13.
[78] P.S.T. Yuen, S.R. Dunn, T. Miyaji, H. Yasuda, K. Sharma, R.A. Star, Am. J. Physiol.-Renal Physiol. 286 (6) (2004) F1116–F1119.